MODELS OF THE SL9 IMPACTS II. RADIATIVE-HYDRODYNAMIC MODELING OF THE PLUME SPLASHBACK

Drake Deming
Planetary Systems Branch, Code 693
Goddard Space Flight Center, Greenbelt, Maryland 20771

and

Joseph Harrington
Department of Astronomy
Cornell University, Ithaca, NY 14853
Received 2000 October 13; accepted 2001 April 17.

ABSTRACT

We model the plume 'splashback' phase of the Shoemaker-Levy 9 (SL9) collisions with Jupiter. We modified the ZEUS-3D hydrodynamic code to include radiative transport in the gray approximation, and present validation tests. After initializing with a model Jovian atmosphere, we couple mass and momentum fluxes of SL9 plume material, as calculated by the ballistic Monte-Carlo plume model of Paper I of this series. A strong and complex shock structure results. The shock temperatures produced by the model agree well with observations, and the structure and evolution of the modeled shocks account for the appearance of high excitation molecular line emission after the peak of the continuum light curve. The splashback region cools by radial expansion as well as by radiation. The morphology of our synthetic continuum light curves agree with observations over a broad wavelength range (0.9–12 μm). Much of the complex structure of these light curves is a natural consequence of the temperature dependence of the Planck function, and the plume velocity distribution. A feature of our ballistic plume is a shell of mass at the highest velocities, which we term the 'vanguard'. Portions of the vanguard ejected on shallow trajectories produce a lateral shock front, whose initial expansion accounts for the 'third precursors' seen in the 2-μm light curves of the larger impacts, and for hot methane emission at early times observed by Dinelli et al. Continued propagation of this lateral shock approximately reproduces the radii, propagation speed, and centroid positions of the large rings observed at 3–4 μm by McGregor et al. The portion of the vanguard ejected closer to the vertical falls back with high z-component velocities just after maximum light, producing CO emission and the 'flare' seen at 0.9 μm. The model also produces secondary maxima ('bounces') whose amplitudes and periods are in agreement with observations.

Subject headings: planets and satellites: Jupiter, comets: P/Shoemaker-Levy 9, infrared: solar system, hydrodynamics, impacts, shock waves

1. INTRODUCTION

In this paper we model the collapse of a nominal ejecta plume from the collision of comet Shoemaker-Levy 9 (SL9) with Jupiter. We couple the mass and momentum fluxes from the ballistic plume model of Harrington & Deming (2001, hereafter Paper I) to a radiative hydrodynamic model of the jovian atmosphere, and we follow the shock formation, evolution, and cooling in detail. The ballistic plume model was developed in Paper I based on the power-law velocity distribution of Zahnle & Mac Low (1994), with free parameters constrained to reproduce the appearance of the observed plumes at the jovian limb and the disk debris patterns as observed by Hammel et al. (1995). In the present model, only a few additional parameters can be varied, and we have simply adopted reasonable values, without attempting to 'fine-tune' the model's agreement with observations. It is not our intent to 'fit' the model to the observations for specific impacts, but merely to elucidate the physics of a typical splashback. Nevertheless, the success of our approach is exemplified by good agreement between our synthetic light curves and observations over a broad wavelength range (0.9 – 12 μm), and by the occurrence in the model output of several phenomena which have previously eluded explanation.

We describe the physical basis of the radiative hydrodynamic model in Sec.2 and its validation using test problems in Sec.3. In Sec.4, we apply it to the nominal SL9 plume, and compare the results to observations. Section 5 summarizes our results.

2. CODE PHYSICS

The radiative hydrodynamic model utilizes the ZEUS-3D hydrocode (Stone & Norman 1992; Clarke et al. 1994), which we have modified to include radiative transport in the gray approximation. The physics in our modified code is given by the fluid equations:

$$\text{Continuity:} \quad \frac{\partial \rho}{\partial t} + \nabla \cdot (\rho \mathbf{v}) = 0 \tag{1}$$

$$\text{Momentum:} \quad \frac{\partial \mathbf{P}}{\partial t} + \nabla \cdot (\mathbf{P v}) = -\nabla p - \rho \mathbf{g} \tag{2}$$

$$\text{Energy:} \quad \frac{\partial e}{\partial t} + \nabla \cdot (e \mathbf{v}) = -p \nabla \cdot \mathbf{v} + 4\pi\kappa\rho(J - S) \tag{3}$$

$$\text{Ideal Gas Equation of State:} \quad p = (\gamma - 1)e = R\rho T, \tag{4}$$

with mass density ρ, time t, velocity flow field $\mathbf{v}$, momentum vector field $\mathbf{P} = \rho\mathbf{v}$, pressure p, (constant) gravitational acceleration vector $\mathbf{g}$, internal energy per unit volume e, opacity κ, mean intensity J, source function S, the (constant) ratio of specific heats γ, gas constant R, and temperature T. We also add the radiative transfer equations:

$$J(\tau_0) = \frac{1}{2} \int_0^\infty S(\tau) E_1(\tau - \tau_0) \mid \tau - \tau_0 \mid d\tau \tag{5}$$

$$S = \frac{\sigma T^4}{\pi} \tag{6}$$

$$\tau = \int \kappa\rho \; dz \tag{7}$$

with optical depth τ, first exponential integral function E_1 (Mihalas 1978), Steffan-Boltzmann constant σ, and height above the 1-bar level in the jovian atmosphere z. Note that our implementation of radiative transfer in ZEUS-3D treats radiation as a *transport mechanism*, not as a *fluid*. We ignore the internal energy and stresses of the radiation itself, and assume its propagation to be instantaneous.

The model uses quadrature integration to calculate J from Eq. 5. Shocked regions occupying only a few grid zones are adequately represented in the quadrature, allowing the correct reproduction of any possible heating of the lower atmosphere by radiation from the overlying shocks (Melosh et al. 1990). Note also that Eq. 6 represents an assumption of local thermodynamic equilibrium (LTE) for the radiation field.

The radiative transfer Eqs. 5–7 require an additional boundary condition, represented by the effective temperature of the atmosphere (T_{eff}) and the consequent radiative flux which passes continuously through the fluid. At the lower boundary of the atmosphere, where $\tau \gg 1$, we utilize the approximations (Mihalas 1978):

$$J - S = \frac{1}{3} \frac{d^2 S}{d\tau^2} \tag{8}$$

$$\frac{dS}{d\tau} = \frac{3\sigma T^4}{4\pi}. \tag{9}$$

In order to implement Eqs. 8 and 9 in the code, we add a 'virtual' layer below the deepest active layer. We calculate the optical depth and temperature of the virtual layer in advance from T_{eff}, and use them in calculating the space-centered derivatives of S with respect to τ. Equation 8 then gives the value of $J - S$ when the optical depth exceeds some pre-determined value (typically 10).

ZEUS uses an explicit finite difference method to integrate the fluid equations, with a Courant condition (Courant & Friedrichs 1948) imposed to limit the size of the time step. Our addition of radiation to the energy equation, and the influx of plume mass and momentum to the top layer of the atmosphere, must also be considered in the context of the ZEUS finite-difference approximations. We re-derived the finite difference approximation to Eq. 3 to maintain correct centering in space and time, and we found that requiring the change in e to be less than 10% from radiation in a single time step gives stable results. We similarly require that the plume mass added to the top atmospheric layer cannot change ρ by more than 100% in a single time step.

The mass and momentum fluxes in the ballistic plume are relatively uniform over a 'core' region defined by the opening angle of the 'launch cone' in $r\theta$ coordinates. ZEUS-3D was therefore configured to solve Eqs. 1–9 in $zr\theta$ geometry, where r is radial distance from the impact point and θ is the azimuthal angle. Given the approximate uniformity in θ for the bulk of the infalling mass, all models presented here use a single 2-D wedge in θ, which provides for the plume's vertical and radial velocity components, and permits buoyancy effects (gravity waves). We neglect Coriolis effects and the curvature of the jovian atmosphere, which will not significantly affect the shock structure and light curves. Figure 1 shows a sketch of the $zr\theta$ geometry as implemented in ZEUS.

Zahnle & Mac Low (1995, hereafter ZM95) computed a theoretical light curve under the assumption that the infalling plume energy was instantaneously balanced by radiative losses. Since radiative losses have a time scale which varies as T^{-3}, a detailed treatment of radiative damping is needed. Radiation in numerous molecular bands and continuum emission from grains are both potentially important. However, the detailed wavelength dependence of the radiation is less important to the hydrodynamics than the bolometric energy loss, so we use a mean opacity. Also, since the scale height of the jovian atmosphere is much less than the radial scale of the plume splashback, we compute the mean intensity at each point under the assumption that the atmosphere is homogenous in r and θ. In other words, the radiation field does not 'see' points at other values of r and θ, only the variation in the z direction is accounted for (this is implicit in Eq. 5).

A significant portion of the plume mass was likely present in the form of silicate or other grains (Nicholson et al. 1995a; Griffith et al. 1997; Molina et al. 1997; Friedson 1998) whose deposition is believed to account for the post-impact debris patterns on the jovian disk. However, Takata & Ahrens (1997), Zahnle (1996), and Paper I calculate that the plumes were mostly entrained jovian air. We assume that the overall hydrodynamics of the splashback was determined by the gaseous component, with grains advected by the flow and heated by the shocks (Moses 1997). Nevertheless, we have incorporated an option in the code for following the motion of tracer grains, by explicit integration of the grain momentum equations. Ballistic studies (Jessup et al. 2000; Harrington & Deming 2001) have shown conclusively that continued radial transport after splashback is necessary to explain the disk debris patterns. We performed exploratory grain transport calculations, which indicated good agreement with the observed radial extent of disk debris, but also convinced us that the transport of grains does not have a major effect on the phenomena discussed in this paper (e.g., light curves).

The original version of ZEUS-3D applies to a single-component fluid, having a single value for R and γ. We adopt $\gamma = 1.2$ from the Galileo observations of the G-impact fireball (Carlson et al. 1997). We also apply this value to the jovian atmosphere, lacking a direct determination for shocked jovian air. However, we have modified ZEUS to use two values for the gas constant (R), consistent with different molecular weights (μ) for the plume material and for jovian air. We use $\mu = 2.28$ g mole^{-1} for jovian air, which reflects the helium abundance from the Galileo Probe Helium Interferometer (von Zahn et al. 1998). For the plume, we calculated μ assuming that the impacting object was predominately water ($\mu = 18$); the fraction of the plume material which was impactor was determined in the ballistic plume modeling, and was not a free parameter in ZEUS-3D. To explore the 'zero-th order' effects of large versus small impacts, we vary the plume mass by a scale factor, keeping the same proportions of impactor and jovian air in the plume.

ZEUS-3D uses a source step and a transport step to integrate the fluid equations (Stone & Norman 1992). The source step accelerates the fluid using the pressure gradient and gravity terms on the right of Eq. 2 and the radiation term on the right of Eq. 3. The transport step integrates the spatial and temporal gradients to advect the fluid variables across the Eulerian spatial grid, based on the van Leer (1977) scheme. Exploratory calculations indicated that there is little mixing at the plume/atmosphere interface in the first hours after impact, so we used the following simplified treatment. We added an additional van Leer advection calculation to ZEUS-3D, tracking the total overlying column density of plume material at each r, thus determining the location of the plume/atmosphere boundary. This permits two values of R, depending on whether the fluid in a given grid zone is plume, atmosphere, or both.

3. CODE VALIDATION

The ZEUS hydrocode has itself been tested well against a suite of standard hydrodynamic test problems (Stone & Norman 1992). Since we have modified the code, we must establish the validity of our modifications and also show that we have not inadvertently interfered with the existing code algorithms. We have performed numerous tests for these purposes, including direct checks of some code algorithms against hand calculations. We also conducted five more-complex tests of the code, as described below.

3.1. *Test 1: Shock Tubes*

The shock tube is a one-dimensional test problem wherein a boundary separates two isotropic regions of different pressures and densities. When the boundary is removed, a shock propagates into the lower pressure region, and the code results can be compared to an analytic solution (Sod 1978). For these tests, we configured ZEUS-3D in a 1-D mode with 1000 zones and with the radiation terms turned off. We first repeated the shock tube test described by Stone & Norman (1992), and verified that we can reproduce their Fig. 11. However, shocks in the SL9 problem will have larger compression ratios, e.g., the jump in pressure across the shock can be as large as 10^4. Figure 2 shows a successful test for this compression ratio.

3.2. *Test 2: Hydrostatic Equilibrium and Scale Height*

The second term on the right of Eq. 2 represents Jupiter's constant gravitational acceleration. To test the addition of this term, we started with a 2-D volume with initial constant pressure but oscillatory temperature and density. Since constant pressure is not a solution to (2), the code evolved this atmosphere. We used the radiative damping option, with the arbitrary constraint that $J = S$ for $T = 500$ K. (This is equivalent to placing an optically-thin atmosphere in a blackbody cavity at this temperature.) At $t = 8 \times 10^5$ sec, a near-equilibrium state with constant temperature and gradients in pressure and density prevailed. We verified that there were no significant horizontal gradients, and the pressure gradient term balanced the $\mathbf{g}\rho$ term to within a fractional error $< 5 \times 10^{-6}$. The scale height agreed with the analytic value to within 0.1%.

3.3. *Test 3: Radiative Damping Time Scale*

The radiative damping time of a temperature perturbation depends on its spatial scale as well as its temperature amplitude. Perturbations of large spatial scale can extend over many optical depths, and these damp slowly because their optical thickness hinders photon transfer. Spiegel (1957) derived an analytic expression for the damping time of small amplitude temperature perturbations in an isothermal atmosphere in LTE. We turned off the gravitational acceleration term in Eq. 2 and configured ZEUS-3D for a 1-D isothermal atmosphere ($T = 5000$ K), with a superposed sinusoidal temperature perturbation of amplitude 100 K. These relatively high temperatures assure that radiative transfer is rapid in comparison to hydrodynamic effects, which are not included in the analytic damping formula. We used 1000 zones having optical thickness of 0.02 per zone. We ran the code for times which are small compared to the e-folding time of the perturbation (so that the fluid was not significantly accelerated), and we computed the damping rate of the perturbation amplitude, $\partial(\Delta T)/\partial t$, from the model output. Figure 2 shows this rate compared to the analytic solution as a function of the wavelength of the perturbation, measured in optical depths, τ_λ. The largest difference between the code and the analytic formula is 6% at $\tau_\lambda = 2$. Since S represents a small perturbation over J (a 100 K perturbation on a 5000 K background), the 6% error in the damping rate (in $J - S$) results from a 0.5% imprecision in the calculation of J by quadrature integration of Eq. 5. This is more than sufficient for the SL9 problem, because $S \gg J$ in the SL9 shocks.

3.4. *Test 4: Radiative Equilibrium*

Mihalas (1978) analytically derives the temperature *vs.* optical depth structure, $T(\tau)$, of a gray radiative equlibrium atmosphere as a function of $T_{\rm eff}$. Our modified code can reproduce this structure. Since the time scale to achieve radiative equilibrium increases greatly with decreasing effective temperature, we conducted this test using $T_{\rm eff} = 5800$ K, a solar temperature. We started with a 2D volume of fluid having a constant temperature (arbitrarily set to 6000 K), and we added a large arbitrary velocity perturbation in both dimensions. After 4.6×10^5 sec of simultation time the fluid had converged to a near-equilibrium state. All state variables were nearly uniform in the r dimension, and ρ and p satisfied hydrostatic balance to within a few parts in 10^7. The $T(\tau)$ relation was closely equal to the analytic formula for a gray radiative equilibrium atmosphere. Figure 2 shows $T(\tau)$ from the code (points) versus the analytic formula (line). The largest error is 20 K, and most layers are within 10 K (about 0.2% error).

3.5. *Test 5: Advection*

ZEUS-3D uses van Leer (1977) advection. As noted earlier, we have added an additional van Leer advection calculation specifically to keep track of the plume portion of the total fluid. We tested this calculation by tailoring our algorithm to track the *total* mass column density at each r, with a large oscillation in the r velocity. The oscillation amplitude was 10 km sec^{-1} at the top of the model, decreasing as $(1 + \tau^2)$. The amplitude was sinusoidal in r, with a wavelength of 10 grid zones. This oscillation provides a greater degree of fluid advection than occurs during the splashback, so it is a stringent test of our van Leer algorithm. Since our algorithm is tracking the same fluid as the original ZEUS algorithm in this case, the two calculations should track closely. After 5000 sec of simulation time, the largest difference between the column densities from the two independent calculations was 0.5%. This accuracy is more than sufficient to track the plume column densities for the time scales of interest here.

4. MODEL RESULTS

4.1. *Input Parameters and Nominal Plume*

Table 1 gives the parameters adopted for our nominal model. Constraints on the ratio of plume to impactor mass come from conservation of energy and the adopted velocity distribution used in the ballistic Monte-Carlo model. Both plume and impactor mass were varied by the same scale factor in the ZEUS modeling (e.g., compare R impact to L impact).

Alexander & Ferguson (1994) calculate Rosseland mean opacities for solar system matter. At typical splashback temperatures ($600 - 2000$ K) the Rosseland mean varies from 2.5 - 0.02 cm^2 g^{-1}. From the composition tabulated by Jessberger & Kissel (1991), the comet's metallicity is enhanced by a factor of 40 over the sun. Hence the opacity for the impactor material will be in the range 100 - 1 cm^2 g^{-1}. We performed exploratory ZEUS calculations with opacity calculated as a function of temperature at each time step, by interpolating in the tabulated values given by Alexander & Ferguson (1994). We find that this does not dramatically improve agreement with observations. We have therefore used a constant intermediate value, 10 cm^2 g^{-1}, independent of temperature and density.

Because the plume is optically thin, varying the mass of the plume has the same (nearly linear) effect on the modeled light curves as varying the opacity. Hence, the impactor mass and opacity do not change (to first order) the *shapes* of our

TABLE 1
MODEL PARAMETERS

Parameter	Value
R-fragment mass	1.7×10^{14} g
L-fragment mass	1.7×10^{15} g
R-plume mass	1.3×10^{15} g
L-plume mass	1.3×10^{16} g
Impactor molecular weight	18.0 g mole^{-1}
Jovian molecular weight	2.28 g mole^{-1}
Impactor opacity	10 cm^2 g^{-1}
Jovian opacity	8×10^{-3} cm^2 g^{-1}
Ratio of specific heats, γ	1.2

modeled light curves, they merely scale the fluxes. To specify a nominal plume mass (Table 1), we matched the peak of the 10-μm modeled curve to the flux of the well-observed R impact (Friedson et al. 1995). Although we have relied on the R-impact to calibrate the mass scaling factor for our models, most of our calculations used an L-fragment mass.

Our nominal plume contains a shell of mass at the highest velocity, and the necessity for this 'vanguard' of mass is discussed in paper I. However, we have also calculated synthetic light curves for a plume wherein the vanguard is eliminated, and a 'non-vanguard' light curve is shown in Sec. 4.6. We adopted an observed temperature profile for the jovian atmosphere derived from Voyager IRIS measurements (Hanel et al. 1979), supplemented by Galileo probe results (Seiff et al. 1996) at the greatest heights. Since this empirical atmosphere is not in gray radiative equilibrium, coupling it to ZEUS introduces unaccounted sources and sinks of energy, but these small imbalances have no significant effect on our results.

How should we couple the plume from the expanding fireball into our splashback model? As the fireball expands to greater heights, it encounters decreased atmospheric pressure, and its internal pressure also decreases greatly. Above some transition height, its motion becomes controlled by ballistics rather than hydrodynamics. Based on the results of Carlson et al. (1997), we infer this to occur at $z \sim 400$ km above the 1$-$bar level. Re-entry of the plume will shock the jovian atmosphere even for $z >> 400$ km, but these shocks at very great height will produce negligible IR emission, and will not deaccelerate the infalling plume significantly. Accordingly, we add the infalling plume mass and momentum fluxes to our model in the layer 400 km above the 1$-$bar level, interpolating these fluxes from the plume model at each ZEUS r value and time step.

The infalling plume is believed to be cold (ZM95), so we have adopted an initial plume temperature of 100 K, this being equal to the upper atmospheric boundary temperature in gray radiative equilibrium. (Our results are not sensitive to the initial plume temperature.) The ZEUS computational boundaries at maximum z and r were configured to be transmitting. The lowest-z surface at the greatest atmospheric pressure (5 bars) was specified as reflecting, although splashback effects do not penetrate even close to this depth. We experimented with a variety of grid spacings in the model, in order to determine a grid configuration which resolves the splashback shocks, while remaining computationally tractable. Our adopted grid uses 20 layers of 10 km thickness in the region below 200 km, 100 layers of 4 km thickness from 200 to 600 km (where the splashback effects are most prominent), and an additional 40 layers of 10 km thickness above 600 km. Our radial grid spacing was 75 km, extending from $r = 0$ to $r = 12000$ km in 160 zones. We verified that finer grid resolution or greater extent will not change our results significantly.

Because the plume is injected into the code at $z = 400$ km, the layers overlying this height participate only minimally by, for example, 'catching' matter which rebounds upward. Accordingly, we do not illustrate these layers in our Figures. Note also that the matter which they contain is counted as plume matter by the advection scheme described in Sec. 2. They initially contain jovian atmosphere, but this accounting error has a negligible effect, since the column density above 400 km is very small.

Since our computations attempt specifically to isolate phenomena related to the splashback, we ignore phenomena related to the $r = 0$ boundary, and we couple to ZEUS only plume material ejected on paths at or above the horizontal. We also ignore the channel created by the entry of the fragment into the atmosphere. Some possible effects of this channel are discussed in Sec. 4.8.

4.2. *Shock Structure and Evolution*

The structure and evolution of splashback shocks has been discussed by Zahnle (1996, hereafter Z96). Our results are generally consistent with Z96's conclusions, but provide additional insights. Figure 3 illustrates our calculations of the shock development and evolution at times extending up to the peak of the main event at 700 seconds post-impact. Each panel is labeled by time and gives a false-color representation of the log of temperature, and also includes overlaid velocity vectors.

At 100 sec, most of the infalling mass has not yet hit the shock and is still cold, producing the dark region filling the upper left corner. But the border of this region is bright, denoting a shock. The shock is hottest at the right edge. At this early time, the infalling plume mass cannot exhibit large z velocities, because large z-velocity material requires longer times for re-entry. But large r velocities are present, especially in the vanguard. Since this shock comes from the highest velocity material, it is hot, and is most easily seen in the ascending branch of light curves at the shortest wavelengths (McGregor et al. 1996; Ortiz et al. 1997), or in strong spectral bands such as 3.3-μm methane (Dinelli et al. 1997), rather than the long thermal wavelengths (Lagage et al. 1995; Livengood et al. 1995). In our synthetic light curves it produces the 'third precursors' noted by McGregor et al. (1996) and other observers. HST imaging of plumes at the limb (Jessup et al. 2000) shows emission attributed to an upward-propagating shock near this time. Upward-propagating shocks from the early plume expansion are deliberately omitted from our model, but the emission seen by Jessup et al. (2000) and the radially-propagating shock modeled in Figure 3 are parts of the same continuous process of plume expansion and splashback.

At 300 seconds enough plume material has fallen to drive a shock down to 200 km above the 1$-$bar level (near $r = 1500$ km), and the lateral shock has now expanded to $r = 4000$ km. Additional infalling plume material now encounters previously-fallen plume, and a second shock begins to propagate back into the infall, as predicted by Z96. This is becoming evident as a warm region above the hottest shock in the $r = 1000 - 3000$ km interval. Note also that for $r < 1000$ km the jovian atmosphere has temporarily rebounded from the pressure of the initial plume infall. This rebound is the first sign of a pressure-mode oscillation which develops in the atmosphere at the acoustic cutoff frequency.

At 700 seconds, near the peak of the observed (and our modeled) light curves, the shock structure is complex. For $r \lesssim 4000$ km the temperature in the shocked plume rises with height. This is due to the existence and evolution of two shocks. The lowest shock occurs near the plume/atmosphere boundary, while the upper shock, due to plume-on-plume collision, has now propagated up to nearly $z = 400$ km. Note also that velocities in the lower shocked region are almost entirely radial, because the z-component velocity has been dissipated in the shock. The reversed temperature gradient occurs because the lower shock cools before the upper shock. At any given time, the lower shock has existed longer, so its cooling has proceeded further. Both shocks are optically thin, and independently cool by radial expansion, as well as by radiation. For a given total velocity, plume mass having the smallest $z-$component and largest $r-$component velocity will fall back first. So the radial expansion of the lower shock is greater than the upper, which contributes greatly to its more rapid cooling.

The lower shock makes the dominant contribution to the IR light curves at this time. Although it is cooler, it has a much greater mass density than the upper shock. As time proceeds, regions of reversed temperature gradient occur at increasingly larger r, and occupy much larger area (in the $zr\theta$ model geometry, surface area is proportional to r^2).

Also at 700 sec, the lateral shock has moved to near $r = 7000$ km. Up to this time, the expansion of the lateral shock is driven in part by continuing infall of plume mass. A cold rarefaction remains behind it at high z (the dark region at the top of the panel near $r = 6000$ km). A complex and interesting mass flow can be discerned in the shock and rarefaction region, as revealed by the velocity vectors. These vectors show the velocity of the *matter*, which is not the same as the velocity of the shock itself. Matter behind the rarefaction (i.e., at smaller r) moves downward (from infall) as it expands radially, reaching a minimum height of $z \sim 320$ km at the same r position as the rarefaction. Ahead of the rarefaction (i.e., at greater r) there is a slight *upward* component to the continued radial expansion. Some of this matter may fall back again at later times, and has been postulated to account for the secondary maxima in the light curves (Mac Low 1996). However, as we will see in Sec. 4.4, another process is principally responsible for the secondary maxima.

Figure 4 shows the structure and evolution of the shocks at times after the peak of the main event. At 1000 sec, the reversed temperature gradient is accentuated by the collapse of the vanguard. The point where the vanguard intersects a given height first begins to move radially inward at 720 sec. The inward motion of the intersection corresponds to ejection zenith angles decreasing from $45 - 0$ degrees, and this mass falls onto previously-impacted plume matter. A high velocity 'plume-on-plume' collision is consistent with the onset of high-excitation CO emission at 720 seconds, in excellent accord with observations (Meadows & Crisp 1995). This collapsing vanguard produces a hot shock, which is visible near $r = 2000 - 3000$ km. Although the velocity of the matter in the vanguard is directed radially outward, the shock produced by its collapse moves radially inward with time. This derives from the ballistics, wherein the last portion of the vanguard to fall back is the portion ejected straight upward, which (having no r velocity) falls back at $r = 0$. As in the case of the lateral shock (which is produced by the horizontally-expanding portion of the vanguard), the shock from the collapsing vanguard is hot, and produces its most significant effects at the shortest wavelengths. It is particularly prominent in our synthetic light curves at 0.9 μm (Sec. 4.3.1), where it accounts for the flare observed to peak near 1000 seconds by several groups (summarized by Ortiz et al. 1997). Model temperatures in the flare shock reach 3000 K. The occurrence of the highest shock temperatures in the collapsing vanguard is qualitatively consistent with CO observations, wherein shock temperature increases monotonically with time until $t \sim 1000$ sec (Kim et al. 1999). The collapse of the vanguard not only provides a temperature sufficient to excite CO overtone transitions (Noll et al. 1997), but also sufficient mass to provide significant optical depth in these lines. Consequently, the 2.3-μm CO features should appear in emission predominately *after* the peak of the continuum light curves, in agreement with observations (Meadows & Crisp 1995). It is not necessary to postulate dust formation preferentially at specific times (Hasegawa et al. 1996) in order to explain the main characteristics of the splashback.

At 1400 sec, infall of *plume* material has ceased, but radial expansion of the fallen plume continues. Collapse of the vanguard leaves a low-pressure wake, which is accentuated by the continued radial expansion. This wake is filled by matter overlying the plume. This in-rushing matter is quite noticeable on the 1400 sec panel, especially in the $r = 2000 - 8000$ km region, where it is seen falling down and outward, joining the radial expansion of the collapsed plume.

In the model, the radial expansion or 'sliding' of the plume is unimpeded by molecular or turbulent viscosity, since viscosity terms are not included in our 'dry water' fluid equations. Under this condition, the plume gas will continue to expand until the layer becomes infinitesimally thin in the z dimension, but particulate grains in the plume will drop below the shock to form a quasi-static debris pattern in the atmosphere. At 1400 seconds, the edge of the radially-expanding plume continues to be marked by the lateral shock, now near $r \sim 12,000$ km. The radial expansion of this shock in the model continues for much greater times, as it becomes essentially a single propagating pressure pulse. Its continued expansion accounts for the rings of large radius observed by McGregor et al. (1996, also Sec. 4.7).

The 2000 sec panel shows that much of the upper atmosphere has cooled significantly, and the level of continuum emission is greatly reduced (i.e., the 'main event' is over). However, even at much later times, residual heating of the upper atmosphere for $z \geq 250$ km remains ~ 200 K, so that many spectral lines will still appear in emission (Bezard 1997; Kostiuk et al. 1996; Lellouch et al. 1995). The lateral shock (now off the panel) continues to propagate to larger radii, as discussed below.

Specific comments should be made concerning the agreement of the modeled shock temperatures with observations. Near maximum light, the cooler portions of the modeled lower shock (600 K at $r = 3000$ km) are in good agreement with the color temperatures seen in the IR continuum (Nicholson et al. 1995a). Regions at larger radius remain warmer than observed (e.g., 1700 K at $r = 5000$ km), but are cooling rapidly. Temperatures in the upper shock produced by the highest

z-velocity material at 1000 seconds (2500 K at $r = 2000$ km) are in good agreement with spectroscopic observations in strong lines (Knacke et al. 1997), but we cannot account for the 5000 K values reported by Kim et al. (1999).

4.3. *Light Curves*

The lack of wavelength-dependent opacities in our modeled light curves limits them. Nevertheless, using the wavelength-dependent Planck function maintains sensitivity of shorter wavelengths to hotter regions, thus accounting for much of the wavelength variation of light curve morphology. Our peak fluxes scale nearly linearly with opacity and with plume mass, because the plume is optically thin. Two factors must be more solidly established in order to derive the impactor masses from the observed light curves. First, the fraction of impact energy (η) which goes into lofting the plume must be known. Second, accurate wavelength-dependent opacities must be incorporated into the model. At present, our adopted values ($\eta = 0.3$ [ZM95] and $\kappa = 10$ cm^2 gm^{-1}) require an impactor mass for the well-observed R fragment of 1.7×10^{14} grams in order to match the 10-μm flux of Friedson et al. (1995). Assuming a mass density of 0.5 g cm^{-3}, the implied diameter of the R fragment is about 400 meters. The mass of the largest fragment (L) would be an order of magnitude larger, based on the 10-μm flux observed by Lagage et al. (1995).

We discuss the comparison between the modeled and observed light curves at several wavelengths spanning the range from just longward of the visible to the thermal IR. We plot the observed and modeled light curves using scales (linear, log, etc.) which follow the style of the observed light curves as originally published. Also, we have also applied an approximate correction for viewing geometry to the theoretical curves. (This correction, while not negligible, is not large enough to be a significant issue in the comparisons.)

4.3.1. *0.9-μm Light Curves*

Several observational groups observed large impacts (L and H) at 0.9 μm, using CCD detector arrays. Ortiz et al. (1997) summarized the observations. Schleicher et al. (1994) obtained the most extensive data, which are re-plotted in Fig. 5. The observations as originally published show a baseline drift toward higher intensities at the latest times. They attribute this baseline increase to greater reflectivity of regions surrounding the splashback site, which is not relevant in this context. We therefore removed the observed baseline using a low-order spline.

The observed light curves at this wavelength show a double-maximum structure. The first maximum is broader, and peaks near 450 seconds, corresponding to the main event. The second maximum is much sharper, and peaks near 1000 seconds. The modeled light curve exhibits both 450 and 1000 second maxima, whose relative widths and amplitudes agree well with the observations. However, the modeled curve also exhibits an additional maximum near 250 sec, which is not seen in the observations.

Radiation at this wavelength is particularly sensitive to the hottest material in the splashback, because of the exponential term in the Planck function. Hot material is especially prominent at two epochs. The first hot epoch begins quite early, as the portions of the vanguard having small $z-$component and large $r-$component velocities produce the lateral shock. Methane observations show high temperatures in this epoch persisting for much longer than can be plausibly ascribed to the fireball phase (e.g., Fig. 6 of Dinelli et al. 1997). The first hot epoch involves the shock heating of the jovian atmosphere as the lateral portions of the vanguard expand. A second hot epoch begins at 720 sec, caused by the collapse of vanguard mass ejected at zenith angles less than 45 degrees. This hot epoch is more familiar to observers; it involves infall onto regions of previously-fallen plume material, which likely accounts for the fact that it is quite prominent in CO (Meadows & Crisp 1995; Kim et al. 1999; Meadows et al. 2001).

The area encompassed by the lateral shock increases as the shock expands, but its temperature decreases. Hence its maximum contribution to short-wavelength light curves occurs at a time ($200-300$ sec) which is determined by the balance between these competing factors. The shoulder on the Fig. 5 modeled light curve (marked 'PC3' for 'third precursor', see Sec. 4.3.2) indicates the maximum contribution of the lateral shock. The observed light curve does not show the PC3 feature, but it is similar to the model in that it exhibits a significant rise almost immediately after impact, which is not seen in observations at longer wavelengths (Nicholson 1996).

The broad peak in the modeled and observed curves near 450 seconds (marked 'ME' for 'main event') corresponds to the main event emission seen at longer wavelengths, which are sensitive to a larger range of temperatures. However, both the model and observations show that the main event at short wavelength is shifted significantly earlier in time, i.e., ~ 450 seconds post-impact *vs.* ~ 700 seconds at longer wavelengths. This derives from the rapid cooling of the lower shock, as discussed in Sec. 4.2.

The second hot epoch corresponds to the sharpest peak in the light curve. This feature has been called the 'flare' by Fitzsimmons et al. (1996) and is marked by 'F' in Fig. 5. We adopt this terminology (note that the same term has been used more generally by some authors to denote the entire period of post-impact brightening). The origin of the flare has not been adequately explained, although Ortiz et al. (1997) correctly identified it with high-velocity ejecta. Our modeled curve accounts well for its amplitude relative to the main event, albeit with a slight error in the timing of the peak. The agreement is too good to be accidental, and we conclude that the model has captured the essential physics of this feature. The flare comes from vanguard material launched on zenith angles less than 45° and begins about 720 sec post-impact. The last portions of the vanguard to re-enter are those launched vertically; for a vanguard velocity of 11.8 km sec^{-1} these fall back at 1015 sec. In the well-known HST limb images (Hammel et al. 1995, replotted in Paper I), the flare corresponds to the 'plume flat on limb' phase of plume collapse. The modeled light curve declines very steeply after this time, reflecting our adopted sharp velocity cutoff. The observed flare occurs somewhat earlier, implying a slightly smaller cutoff velocity for this impact. The more gradual decline in the observed flare also suggests that the velocity cutoff in the real plume was not quite so sharp as in the model, i.e., the outer edge of our modeled vanguard is too sharp. Models which eliminate the vanguard entirely do not produce an acceptable flare phase in their 0.9-μm light curves.

4.3.2. *2-μm Light Curves*

Figure 6 shows the light curve observed for the G impact by McGregor et al. (1996), plotted on a log scale in comparison to our modeled light curve. The morphologies of these light curves are very similar to each other, again indicating that the model is accounting to a large degree for the splashback physics. Essentially all features of the observed light curve find counterparts in the model. These are marked PC3 (third precursor), ME (main event), F (flare), B (bounce), and 2B (second bounce). The PC3 feature was identified in the observations by McGregor et al. (1996). The presence of third precursors on the ascending branches of short-wavelength light curves is a natural consequence of the expansion of the lateral shock, as discussed in Sec. 4.3.1. In Fig. 6, the observed PC3 immediately follows the second precursor (from the fireball), which we do not model with ZEUS.

Both the modeled and observed light curves exhibit a broad main event phase between 500 and 1000 sec. Both ME features are similar in that they decline more sharply than they ascend. This is due to the sudden collapse of the vanguard in the flare phase; in the modeled light curve this creates a particularly sharp drop in intensity near 1000 sec. This bears an especially strong resemblence to observations of the K impact (McGregor et al. 1996; Watanabe et al. 1995), but is unlike Keck observations of the smaller R impact (Graham et al. 1995), which show a smoother and more symmetric main event. A tendency toward smoother light curves for smaller impacts was previously noted by ZM95, and may indicate the lack of a vanguard for smaller plumes (see Sec. 4.6).

Both light curves exhibit a secondary peak (the bounce) about 500–600 sec after the main event peak. Understanding this feature was the original motivation for our work. It is discussed in detail in Sec. 4.4.

There is one significant difference between the modeled and observed light curves of Fig. 6. The modeled curve decays at a significantly greater overall rate following the main event peak. To some extent this may be due to saturation in the observed fluxes near peak (McGregor et al. 1996), but it is also likely that the model cooling rate, which occurs via radial expansion and radiative damping, is too large. Since the model does not include viscous friction, the plumes expand too rapidly in the model as compared to the observations (see Sec. 4.7). Because radiation at this wavelength is quite temperature-sensitive, a too-rapid rate of cooling will be quite noticeable. Inclusion of viscosity and wavelength-dependent opacities in a future version of the model should allow us to refine the agreement with observations.

4.3.3. *12-μm Light Curves*

Figure 7 shows the light curve observed for the H impact by Lagage et al. (1995), in comparison to our model. We again see good agreement. The predominant feature of thermal-IR light curves is their relatively slow rate of descent following the main event peak. This produces an asymmetry wherein the rise to the main event occurs more rapidly than the decline. The model reproduces this behavior; the intensity near 2000 seconds, relative to the peak intensity, is very similar in the two curves.

Two differences between the modeled and observed light curves are noticeable on Fig. 7. First, the main event is too broad in the model relative to the observations. Second, a weak flare feature remains evident in the modeled light curve. While the flare is a dominant feature in both model and observations at the shortest wavelengths (Fig. 5), it does not appear in the observations at 12 μm. The modeled flare exhibits the same qualitative behavior, being more prominent at shorter wavelengths, but does not fade sufficiently at this long thermal wavelength; this discrepancy could well derive from our crude gray opacity.

4.4. *The 'Bounce'*

Both the modeled and observed light curves in Figs. 6 and 7 exhibit a secondary maximum, or bounce, at ~ 600 seconds following the main event ($\sim 1200 - 1400$ seconds post-impact). The modeled bounces are similar in amplitude to the observations, and at least the first bounce occurs at the correct time in the model. Given the strong similarity between the model and observations, we will look to the model to shed light on the physical cause of this phenomenon.

We have investigated the nature of the modeled bounces extensively. We extended the height of the top boundary in the models (as high as 2000 km), in order to be certain that material which rebounds upward is not lost via model boundary conditions. We used a variety of jovian model atmospheres in order to evaluate the sensitivity to atmospheric parameters. We discuss several potential causes of this phenomenon.

A widely-accepted explanation for the bounce (e.g., Mac Low (1996), Z96) is matter deflected upward from the splash-back shocks, falling back ballistically at later times. However, this matter is deflected upward at relatively shallow angles, reminiscent of a stone skipped across the surface of a pond, and its re-entry is not the principal contributor to the bounce. Instead, the principal cause of the modeled bounce is seen on Fig. 4, in the 1400 second panel, the time of the bounce peak. As noted in Sec. 4.2, the collapse of the vanguard leaves a low-pressure wake which is accentuated by the radial expansion of the plume. Matter rushes into this wake from the zones having $z \geq 400$ km. As this matter hits regions of increased density near $z \sim 300$ km, it is also shocked and moderately heated. If a reservoir of jovian air were available above the collapsing plume, this mechanism would explain not only the light curve bounces, but also the relative prominence of methane and molecular hydrogen quadrupole emission in the bounce phase (Meadows et al. 2001). However, the initial expansion of the fireball may sweep aside, or entrain, much of the overlying jovian atmosphere. Our current model cannot determine whether sufficient jovian air remains above the plume to promptly fill the wake of the vanguard collapse, since the answer depends on the physics of the fireball/plume expansion.

Yet another 'bounce mechanism' derives from the reaction of the underlying atmosphere to the plume infall. As noted in discussion of Fig. 3, the varying pressure of the overlying plume induces an oscillation in the underlying atmosphere at the acoustic cutoff period. This is a natural resonance of a stratified atmosphere in pressure equilibrium (Lamb 1945). For a constant scale height (H) the acoustic cutoff period is $4\pi H/c$, proportional to $T^{1/2}$, where c is the sound speed and T is temperature. We ran a series of computations using several isothermal jovian atmospheric models, with different temperatures. We verified that the oscillation period in the model varies in proportion to $T^{1/2}$. For our empirical model the resonance occurs at $\sim$ 450 seconds. The acoustic mechanism contributes to the modeled bounce, but determines the bounce period only after the first or second maximum. Since the initial portion of the bounce phenomenon has a somewhat longer period (500–600 sec), we expect that the period of the bounce in observed light curves should shorten slightly with time. Nicholson et al. (1995b) observed multiple bounces, but their observations contain gaps which make it difficult to discern variations in the bounce period.

4.5. *Radiative Damping*

The fact that the splashbacks were bright in infrared radiation suggests that radiative emission may be an important, even dominant, cooling mechanism. Is the overall morphology of the light curves determined by radiative cooling of the splashback regions?

Figure 8 shows the effect on the 2-μm light curve of turning off the radiative damping term in the model. In the absence of radiative damping, the peak flux is larger by a factor of 6 (0.8 in log flux). Ignoring the obvious contradiction (that the radiated flux is greater when we turn off radiation), we use this comparison to evaluate the effects of radiative damping on the splashback energy budget. At 2000 seconds post impact, the flux in the nominal model has fallen by two orders of magnitude, whereas the undamped model shows a decrease of 0.6 in log flux (this being due to radial expansion). In the case of the 10-μm light curve (not illustrated), the nominal model falls by only 0.6 in log flux at 2000 sec, versus 0.3 for the undamped model. So the effect of radiative damping, relative to cooling by expansion, is greatest at the shortest wavelengths. ZM95 invoked an instantaneous balance between the kinetic energy of the infalling plume and radiative losses. Our calculations confirm that this is a reasonable approximation. However, the opposite approximation, where radiation is entirely neglected and cooling occurs only by radial expansion, also produces light curves whose *shapes* match the observations fairly well (e.g., Fig. 8, dashed line), especially for the longer thermal wavelengths.

Radiative damping affects the time of maximum in the light curves by a small, yet significant, amount. Maximum of the nominal light curve shifts slightly earlier than in the undamped case. This is due to the greater radiative losses from the hottest shocks, which occur after 720 seconds.

We monitored the modeled temperature profile of the atmosphere below the depth of shock heating. For the largest impacts (L, G, K) this depth corresponds to $p \sim 0.5$ mbar, while for the moderate R impact it is $p \sim 0.1$ mbar. Atmospheric temperatures at greater pressures did not vary significantly (< 1 K), indicating that heating of the lower atmosphere by radiation from the overlying shocks was negligible. The *optical thinness* of SL9 shocks contrasts with the larger terrestrial K/T impact, where radiation from the splashback is believed to have ignited global terrestrial fires (Melosh et al. 1990).

4.6. *Non-vanguard Light Curve*

Figure 8 also shows the 2-μm light curve which results from a plume wherein the vanguard is eliminated. This causes the main event to be more 'rounded' and symmetric, whereas observations of the G and K impact show main events which decline more steeply than they ascend (McGregor et al. 1996; Watanabe et al. 1995). The bounce is broadened and delayed without the vanguard, and as noted in Sec. 4.3.1, the vanguard is needed to match the flare seen at 0.9 μm. Quite a few of the smaller fragments show symmetric main events (e.g., Graham et al. 1995), and were not observed at 0.9 μm, so non-vanguard models might be preferred in those instances.

4.7. *The 3–4-μm Ring*

McGregor et al. (1996) describe the expansion of a large ring seen at 3–4 μm but not at shorter or longer wavelengths. Observations of the ring $\sim$ 4700 and 7400 sec post-impact show radii of $\sim 14,000$ and 18,000 km, respectively. The center of the ring is offset from the impact location in the approximate direction of the incoming fragment by 3600 km. Extrapolating the ring radius at the two observed times back to $t = 0$ suggests an origin near $r = 8000$ km from the impact site. Our model explains these effects, as discussed below.

The lateral shock produced by the vanguard accounts qualitatively for the observed characteristics of this ring. The shock produces a relatively narrow, high-contrast feature, and remains sufficiently hot to the large ring radii. The initial velocity of the vanguard is 11.8 km sec^{-1}, which is much faster than the observed expansion velocity of the ring. However, the shock moves more slowly than the velocity of the matter which matter which impacts it, the plume mass being diverted upwards as it transfers only a fraction of its momentum to the shock. Also, the shock slows as it propagates to larger radius, because the expansion does work against the ambient atmosphere. Linearly extrapolating two observations of ring position back to $t = 0$ may suggest $r = 8000$ km as a starting position, but the velocity is not constant, and the ring likely originated at $r = 0$.

The offset between the ring center and the impact site is also illusory. Because the plume cone is tilted relative to vertical, the lateral shock in the fragment-entry direction is driven by a larger $r-$component velocity, and will expand faster than in the anti-fragment direction. This results in the apparent center of the ring being substantially shifted toward the fragment direction. We calculated the shock positions and propagation speeds at larger radii by running the code in a grid with r extending to 30,000 km. In principle this calculation should be done in full 3-D geometry at this radius, but that is beyond our current computational capabilities. We can closely approximate the results of a 3-D calculation by extracting the infalling plume momentum and energy in 2-D 'slices' in opposite radial directions from the impact point. Figure 9 shows the ring radius and offset from these calculations, compared to the observations by McGregor et al. (1996). The model produces a radius which is too large by about 35% compared to the observations. The offset, conversely, is too small in the model by 50%. The modeled ring velocity between the two observed times is about 2.2 km sec^{-1}, versus an observed velocity of 1.4 km sec^{-1}.

The expansion of the modeled ring is determined solely by the non-viscous fluid Eqs. 1–9, whereas friction from molecular and turbulent viscosity should also be included in future models. The addition of friction from this source can only slow the modeled ring, and will improve the agreement with observations.

The temperature of the modeled lateral shock at the large radii corresponding to the ring observations is ~ 600 K. This is sufficient to produce thermal emission at the 3–4 μm wavelength of the observations. The steep decline in the Planck function makes such emission less detectable at significantly shorter wavelengths, and optical thinness makes the emission faint at any wavelength outside of strong spectral features. McGregor et al. (1996) discussed the peak wavelength of the ring emission, which they concluded was extended longward of the 3.3-μm methane band. Also, the ring was not visible at 2.3 μm, although a methane band occurs at that wavelength. This has prompted investigation of organic compounds such as tholins (Wilson & Sagan 1997). But many observations show (and our models agree) that the splashback took place at quite low pressure levels (less than tens of μbar). This insures that thermal emission from the ring was optically thin, and most easily observed in *strong* bands of *abundant* compounds such as the 3.3-μm fundamental band of methane. In this respect, note that the 2.3-μm methane band has a strength which is nearly two orders of magnitude less than the fundamental (Pugh & Rao 1976), so a 600 K methane ring should not be visible at 2.3 μm. But the 3.3-μm band will exhibit emission in high-J transitions at longer wavelength. For example, the P(18) and P(19) methane lines near 3.5 μm were observed for the C impact by Dinelli et al. (1997). We therefore strongly suspect that the emission of the 3–4-μm ring was indeed due to methane in the 3.3 μm band.

4.8. *Other Phenomena*

As demonstrated in previous sections, our splashback model explains and ties together many of the observed SL9 features. Consequently, we regard as significant the fact that it does not produce the slowly-moving (~ 400 m sec^{-1}) dark rings which Ingersoll & Kanamori (1995) attribute to gravity waves trapped in a deep water layer. Since the large oxygen abundance predicted by the Ingersoll & Kanamori (1995) model was not confirmed by the Galileo probe (Niemann et al. 1998), the origin of these rings remains an open question. Recently, Walterscheid et al. (2000) produced outward-moving gravity waves of the correct speed, using a hydrodynamic model wherein energy is deposited in a cylindrical region with a radius from 250 to 1000 km, extending downward to pressures of $p \sim 0.2$ bars. They cite the plume splashback as the source of this energy deposition.

Our model allows gravity wave generation and propagation, but we find no significant gravity waves excited by the splashback when energy and momentum are coupled ballistically to the top layer of the atmospheric model, as is correct purely for the splashback phase. Splashback effects do not penetrate even close to 0.2 bars, and we suggest that the energy deposition adopted by Walterscheid et al. (2000) would be more realistically ascribed to the entry of the fragment and/or the initial expansion of the fireball. The hot fireball provided a large source of buoyancy which could potentially generate gravity waves at the stratospheric level, and we would not see these gravity waves in our current results.

5. SUMMARY

We have modeled the interaction of SL9 ejecta plumes with the jovian atmosphere during the splashback phase. We treat the plumes as cold matter in ballistic flight, using a Monte-Carlo method to populate the Zahnle & Mac Low (1994) power-law velocity distribution. Included in our nominal plume is a shell of mass near the high-velocity cutoff, which we call the vanguard. Paper I optimized the plume parameters by comparing synthetic model images with HST images of the impact sites.

In this paper, we have coupled the ballistic Monte-Carlo plumes to the ZEUS-3D hydrocode, which we have modified to include radiative damping in the gray approximation. We validated the modified code by comparing its output to analytic solutions for several test problems. Using the code to follow the plume-atmosphere interaction has provided new insights into the physics of a typical splashback. The models explain most of the major observed features of the SL9 light curves and spectroscopy (especially for the larger impacts), including several previously unexplained phenomena. Continuum light curve morphology from the model agrees with observations from 0.9–12 μm, without invoking *ad hoc* hypotheses such as dust formation at specific times.

The plumes include matter ejected nearly horizontally. The horizontally-driven portion of the vanguard produces a lateral shock, which at 200–300 sec post-impact produces hot methane emission as it expands through the atmosphere. Thus commences an early hot epoch in the light curves, most noticeable at the shortest wavelengths. The third precursor phenomenon noted by McGregor et al. (1996) is due to this shock, as is the hot methane emission observed by Dinelli et al. (1997), and the rapid rise in light curves at 0.9 μm (Ortiz et al. 1997). Continued expansion gradually cools this shock, but it maintains a ring-like morphology in the model. This accounts for the rings seen in 3–4-μm images by

McGregor et al. (1996). However, the radius of our modeled ring is 35% greater than the observed ring, and its expansion velocity about two hours post-impact is 2.2 km $\sec^{-1}$ versus the observed velocity of 1.4 km $\sec^{-1}$. The future inclusion of molecular and turbulent viscosity in the hydrocode will slow the modeled expansion, bringing the modeled and observed ring into closer agreement.

Shock temperatures and structure produced by the model agree well with inferences from spectroscopic observations. The first plume matter to fall back produces a shock at the greatest pressures (typically tens of μbars), with shock temperatures briefly approaching 2000 K. Continued infall extends this to a second shock at greater heights, while the lower shock cools rapidly by radiation and by its greater radial expansion. This more-rapid cooling of the lower shock accounts for the bivariate nature of the shock temperatures derived from observations (Nicholson 1996). Just after the peak of the light curve, the lower shock has cooled sufficiently so that a fully reversed temperature gradient is present. A second hot epoch commences at this time (720 sec), with the infall of vanguard matter ejected at zenith angles less than 45°. At these ejection angles, the infalling vanguard collides with previously-fallen plume matter. This 'plume on plume' collision produces shock temperatures as high as 3000 K, and is responsible for the high-excitation CO emission seen at these times. The second hot epoch climaxes near 1000 sec, as portions of the vanguard ejected at small zenith angles are the last to fall back, and the HST limb images exhibit the 'plume flat on limb' phase of plume collapse. This produces the previously-unexplained sharp spike in 0.9-μm light curves, which Fitzsimmons et al. (1996) have termed the flare.

Collapse of the vanguard creates a low-pressure wake, which is further accentuated by the radial expansion of the plume. If sufficient jovian air is left in the immediate wake of the plume collapse, it will rush into this wake, and be moderately shock heated, producing hydrogen quadrupole emission, methane emission, and the secondary light curve maximum called the bounce. Although the timing of the first bounce (500–600 seconds after the main event) is initially determined by this mechanism, subsequent bounces in the model occur at shorter periods (450 sec). This shortening of the period occurs because the underlying atmosphere begins to oscillate at the acoustic cutoff period.

Radiative damping contributes significantly to the cooling of the heated plume, as does the radial expansion of the splashback regions. Radiative damping is more rapid at the highest temperatures, so it acts to limit temperatures of the hottest shocks, and is especially important in shaping light curves at the shortest wavelengths. Following the main event, residual heating in the upper atmosphere is of order 200 K, in approximate agreement with observations (Bezard 1997). Heating of the atmosphere below $\sim$ 1 mbar, by downward radiation from the overlying shocks, is negligible.

We thank K. Zahnle and M.-M. Mac Low for discussions relevant to SL9 modeling, and G. Bjoraker for spectroscopic data. P. Lagage, T. Livengood, P. McGregor, P. Nicholson, J. Ortiz, and H. Schleicher graciously sent us their data in digital form. We are grateful to an anonymous referee, whose diligent review improved the presentation of our results. A portion of this work was performed while J. H. held a NAS/NRC Research Associateship at Goddard Space Flight Center. This research was supported by the NASA Planetary Atmospheres program.

REFERENCES

Alexander, D. R. & Ferguson, J. W. 1994, ApJ, 437, 879
Bezard, B. 1997, Plan. Space Sci., 45, 1251
Carlson, R. W., Drossart, P., Encrenaz, T., Weissman, P. R., Hui, J., & Segura, M. 1997, Icarus, 128, 251
Clarke, D. A., Norman, M. L., & Fiedler, R. A. 1994, Zeus-3D User Manual, University of Illinois at Urbana-Champaign
Courant, R. & Friedrichs, K. O. 1948, Supersonic Flow and Shock Waves, Pure and Applied Mathematics (New York: Interscience)
Dinelli, B. M., Miller, S., Achilleos, N., Lam, H. A., Cahill, M., Tennyson, J., Jagod, M., Oka, T., Hilico, J., & Geballe, T. R. 1997, Icarus, 126, 107
Fitzsimmons, A., Andrews, P. J., Catchpole, R., Little, J. E., Walton, N., & Williams, I. P. 1996, MNRAS, 278, 781
Friedson, A. J. 1998, Icarus, 131, 179
Friedson, A. J., Hoffmann, W. F., Goguen, J. D., Deutsch, L. K., Orton, G. S., Hora, J. L., Dayal, A., Spitale, J. N., Wells, W. K., & Fazio, G. G. 1995, Geophys. Res. Lett., 22, 1569
Graham, J. R., de Pater, I., Jernigan, J. G., Liu, M. C., & Brown, M. E. 1995, Science, 267, 1320
Griffith, C. A., Bezard, B., Greathouse, T. K., Kelly, D. M., Lacy, J. H., & Noll, K. S. 1997, Icarus, 128, 275
Hammel, H. B., Beebe, R. F., Ingersoll, A. P., Orton, G. S., Mills, J. R., Simon, A. A., Chodas, P., Clarke, J. T., de Jong, E., Dowling, T. E., Harrington, J., Huber, L. F., Karkoschka, E., Santori, C. M., Tiogo, A., Yeomans, D., & West, R. A. 1995, Science, 267, 1288
Hanel, R., Conrath, B., Flasar, M., Kunde, V., Lowman, P., Maguire, W., Pearl, J., Pirraglia, J., Samuelson, R., Gautier, D., Gierasch, P., Kumar, S., & Ponnamperuma, C. 1979, Science, 204, 972
Harrington, J. & Deming, D. 2001, ApJ, submitted
Hasegawa, H., Takeuchi, S., & Watanabe, J. 1996, Icarus, 121, 311
Hawley, J. F., Wilson, J. R., & Smarr, L. L. 1984, ApJ, 277, 296
Ingersoll, A. P. & Kanamori, H. 1995, Nature, 374, 706
Jessberger, E. K. & Kissel, J. 1991, in IAU Colloq. 116, Comets in the Post-Halley Era, Vol. 2, ed. R. Newburn, M. Neugebauer, & J. Rahe (Dordrecht: Kluwer), 1075
Jessup, K. L., Clarke, J. T., Ballester, G. E., & Hammel, H. B. 2000, Icarus, 146, 19
Kim, S. J., Ruiz, M., Rieke, G. H., Rieke, M. J., & Zahnle, K. 1999, Icarus, 138, 164
Knacke, R. F., Fajardo-Acosta, S. B., Geballe, T. R., & Noll, K. S. 1997, Icarus, 125, 340
Kostiuk, T., Buhl, D., Espenak, F., Romani, P., Bjoraker, G., Fast, K., Livengood, T., & Zipoy, D. 1996, Icarus, 121, 431
Lagage, P. O., Galdemard, P., Pantin, E., Jouan, R., Masse, P., Sauvage, M., Olofsson, G., Huldtgren, M., Nordh, L., Belmonte, J. A., Regulo, C., Rodriguez Espinosa, J. M., Vidal, L., Mosser, B., Ulla, A., & Gautier, D. 1995, Geophys. Res. Lett., 22, 1773
Lamb, H. 1945, Hydrodynamics (New York: Dover Publications)
Lellouch, E. B., Bezard, B., Moreno, D., Bocklee-Morvan, P., Colom, J., Crovisier, M., Gautier, A., Marten, A., & Paubert, G. 1995, Plan. Space Sci., 45, 1203
Livengood, T. A., Kaufl, H. U., Kostiuk, T. K., Bjoraker, G. L., Romani, P. N., Wiedemann, G., Mosser, B., & Sauvage, M. 1995, in ESO Conf. and Wrokshop Proc. 52, European SL-9/Jupiter Workshop, ed. R. West & H. Bönhardt (Garching bei München, Germany: European Southern Observatory), 137
Mac Low, M.-M. 1996, in IAU Colloq. 156, The Collision of Comet Shoemaker-Levy 9 and Jupiter, ed. K. S. Noll, H. A. Weaver, & P. D. Feldman (Cambridge, UK: Cambridge University Press), 157
McGregor, P. J., Nicholson, P. D., & Allen, M. G. 1996, Icarus, 121, 361
Meadows, V. & Crisp, D. 1995, in ESO Conf. and Wrokshop Proc. 52, European SL-9/Jupiter Workshop, ed. R. West & H. Bönhardt (Garching bei München, Germany: European Southern Observatory), 239–244
Meadows, V., Crisp, D., Barnes, J., Orton, G., & Spencer, J. 2001, Icarus, 999, 99
Melosh, H. J., Schneider, N. M., Zahnle, K. J., & Latham, D. 1990, Nature, 343, 251
Mihalas, D. 1978, Stellar Atmospheres (2nd ed.; San Francisco: W. H. Freeman and Co.)
Molina, A., Moreno, F., & Munoz, O. 1997, Icarus, 127, 213
Moses, J. I. 1997, J. Geophys. Res., 102, 21619

Nicholson, P. D. 1996, in IAU Colloq. 156, The Collision of Comet Shoemaker-Levy 9 and Jupiter, ed. K. S. Noll, H. A. Weaver, & P. D. Feldman (Cambridge, UK: Cambridge University Press), 81
Nicholson, P. D., Gierasch, P. J., Hayward, T. L., McGhee, C. A., Moersch, J. E., Squyres, S. W., van Cleve, J., Matthews, K., Neugebauer, G., Shupe, D., Weinberger, A., Miles, J. W., & Conrath, B. J. 1995a, Geophys. Res. Lett., 22, 1617
—. 1995b, Geophys. Res. Lett., 22, 1613
Niemann, H. B., Atreya, S. K., Carignan, G. R., Donahue, T. M., Haberman, J. A., Harpold, D. N., Hartle, R. E., Hunten, D. M., Kasprzak, W. T., Mahaffy, P. R., Owen, T. C., & Way, S. H. 1998, J. Geophys. Res., 103, 22831
Noll, K. S., Gilmore, D., Knacke, R. F., Womack, M., Griffith, C. A., & Orton, G. 1997, Icarus, 126, 324
Ortiz, J. L., Orton, G., Moreno, F., Molina, A., Larson, S., & Yanamandra-Fisher, P. 1997, A&A, 324, 357
Pugh, L. A. & Rao, K. N. 1976, Molecular Spectroscopy: Modern Research, Vol. II (Academic Press)
Schleicher, H., Balthasar, H., Knolker, M., Schmidt, W., & Jockers, K. 1994, Earth Moon and Planets, 66, 13
Seiff, A., Kirk, D. B., Knight, T. C. D., Mihalov, J. D., Blanchard, R. C., Young, R. E., Schubert, G., von Zahn, U., Lehmacher, G., Milos, F. S., & Wang, J. 1996, Science, 272, 844
Sod, G. A. 1978, J. Comp. Phys., 27, 1
Spiegel, E. A. 1957, ApJ, 126, 202
Stone, J. M. & Norman, M. L. 1992, ApJS, 80, 753
Takata, T. & Ahrens, T. J. 1997, Icarus, 125, 317
van Leer, B. 1977, J. Comp. Phys., 23, 276
von Zahn, U., Hunten, D. M., & Lehmacher, G. 1998, J. Geophys. Res., 103, 22815
Walterscheid, R. L., Brinkman, D. G., & Schubert, G. 2000, Icarus, 145, 140
Watanabe, J., Yamashita, T., Hasegawa, H., Takeuchi, S., Abe, M., Hirota, Y., Nishihara, E., Okumura, S., & Mori, A. 1995, PASJ, 47, L21
Wilson, P. D. & Sagan, C. 1997, Icarus, 129, 207
Zahnle, K. 1996, in IAU Colloq. 156, The Collision of Comet Shoemaker-Levy 9 and Jupiter, ed. K. S. Noll, H. A. Weaver, & P. D. Feldman (Cambridge, UK: Cambridge University Press), 183
Zahnle, K. & Mac Low, M. 1994, Icarus, 108, 1
—. 1995, J. Geophys. Res., 100, 16885

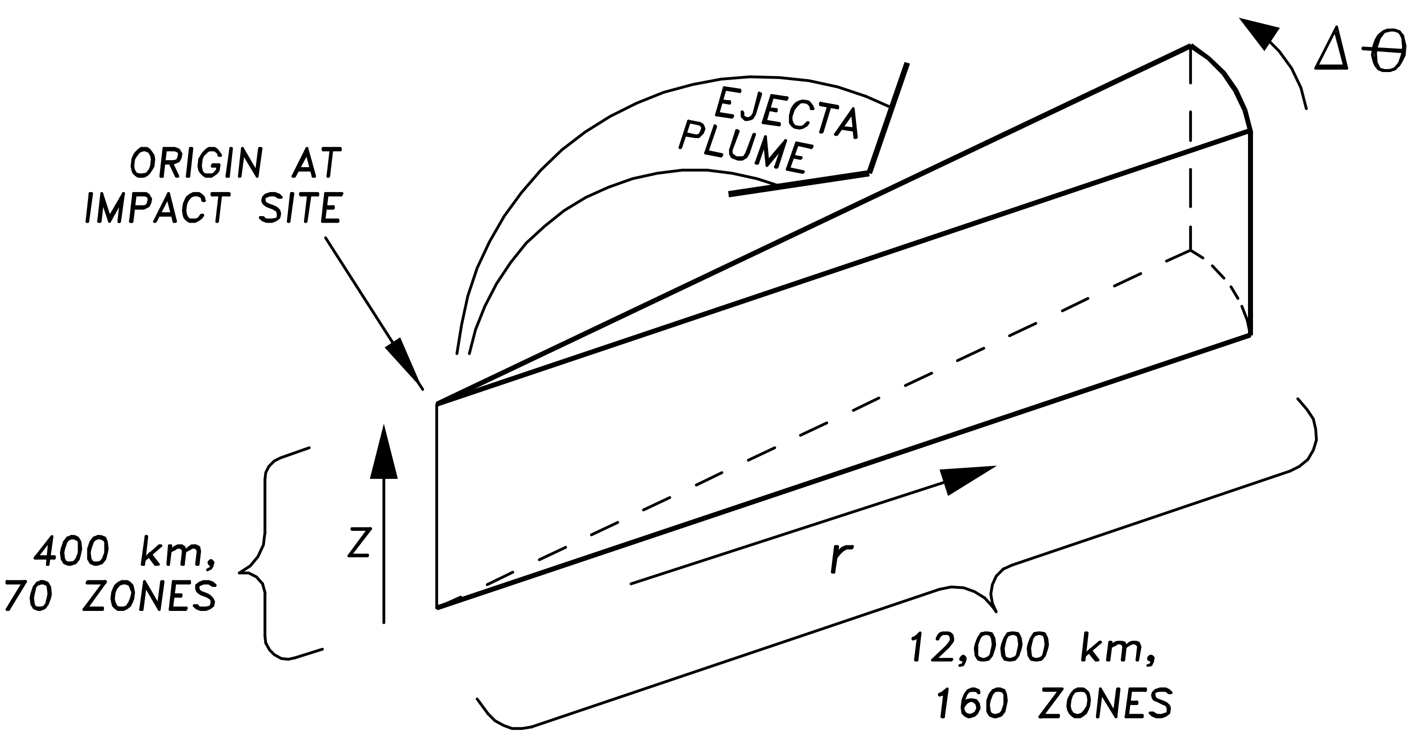

FIG. 1.— Geometry used in the radiative-hydrodynamic model.

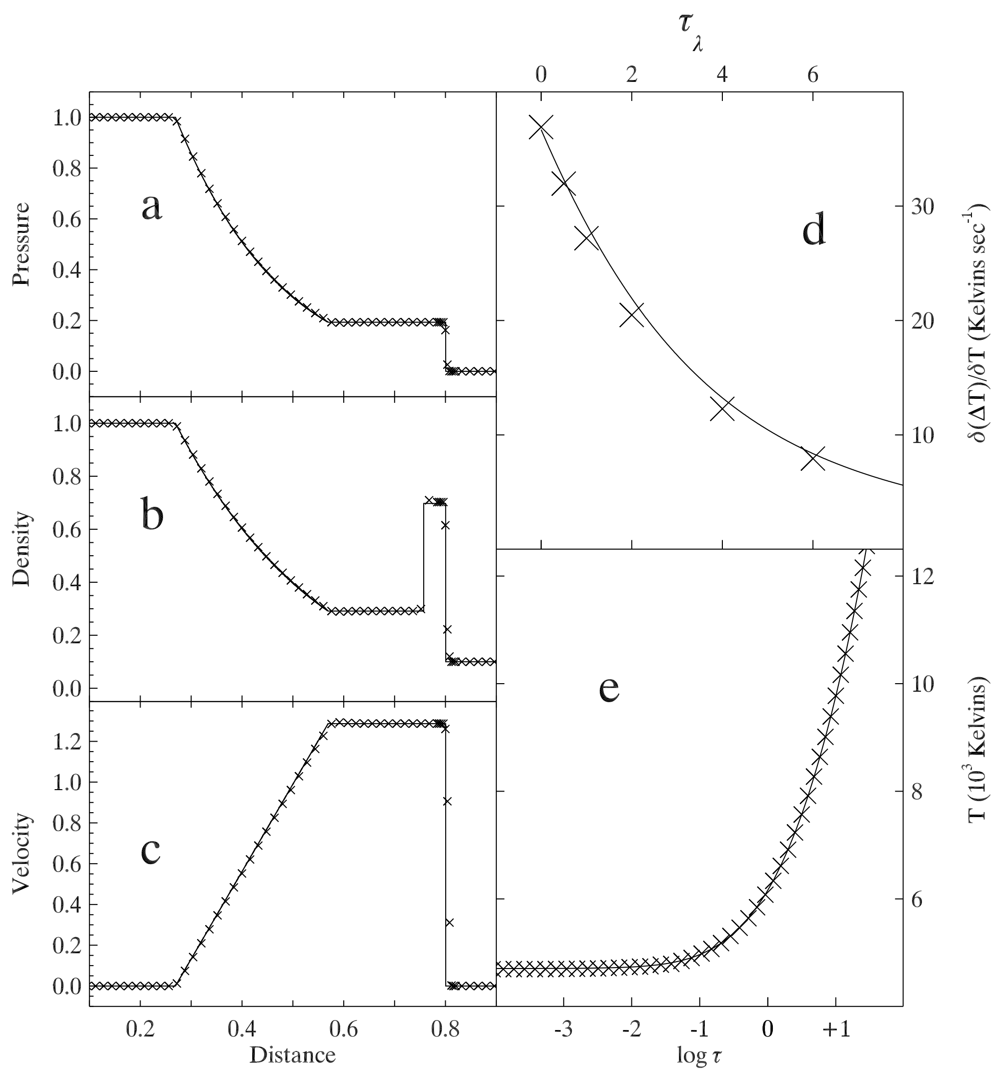

FIG. 2.— a-c) Sod shock-tube test, using dimensionless units. The initial values for p and ρ were both 1.0 on the left of the computational boundary at $x = 0.5$, and 10^{-4} and 10^{-1} respectively on the right of the boundary. The boundary was removed at $t = 0$, and the figure illustrates the computational state at $t = 0.2$. The points show the ZEUS-3D results, and the solid line is the analytic solution calculated following Hawley et al. (1984). d) Radiative damping time scale test. The line represents the analytic formula for the damping rate of temperature perturbations whose spatial wavelength is τ_λ optical depths, and the points are the results from the code. e) Radiative equilibrium test. The line is the analytic temperature *vs.* optical depth relation for a gray atmosphere having $T_{\rm eff} = 5800$ K, and the points are the results from the code.

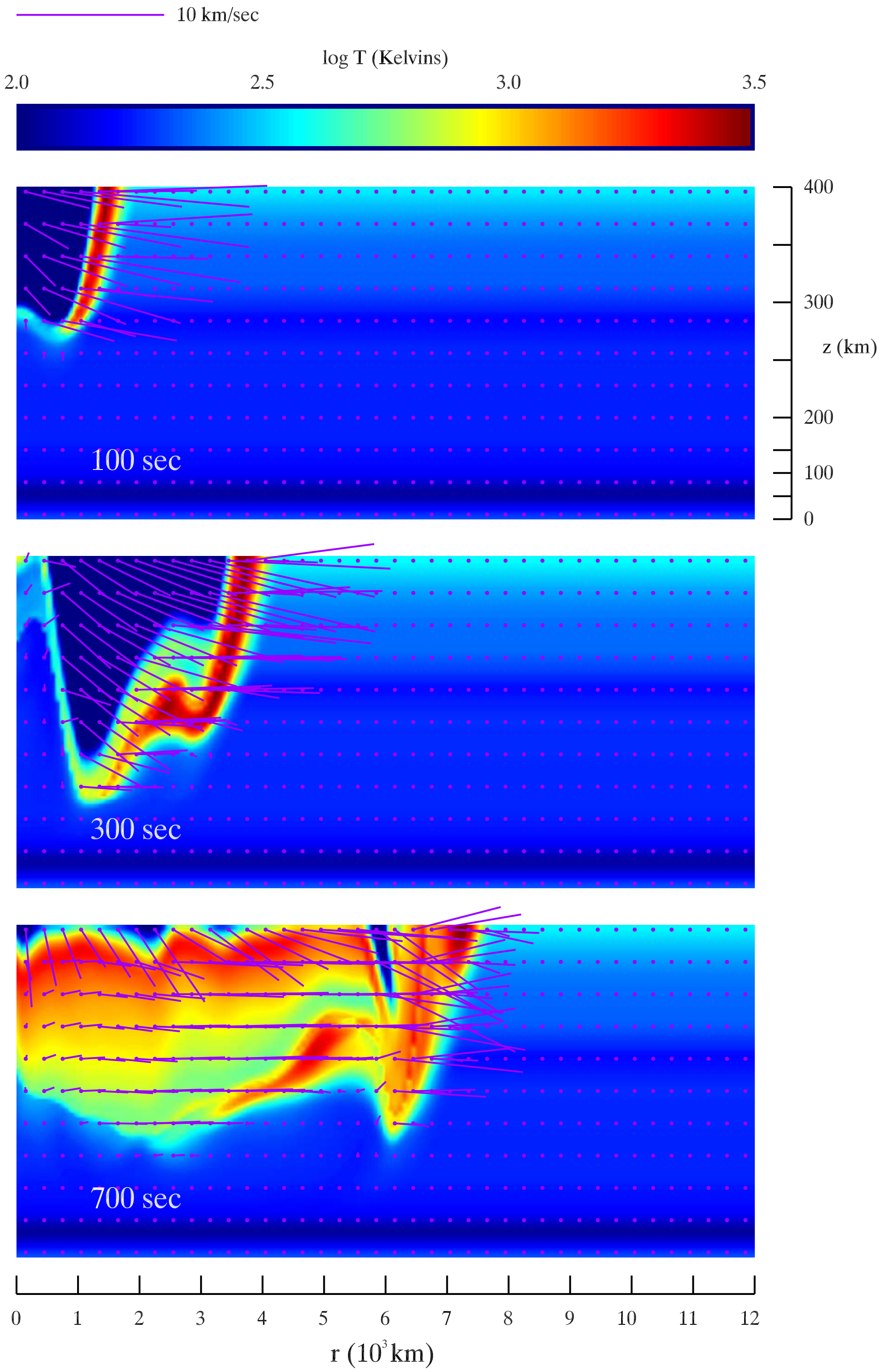

FIG. 3.— Temperature and velocity in the splashback of a large impact (e.g., L) at three times leading to the peak of the main event.

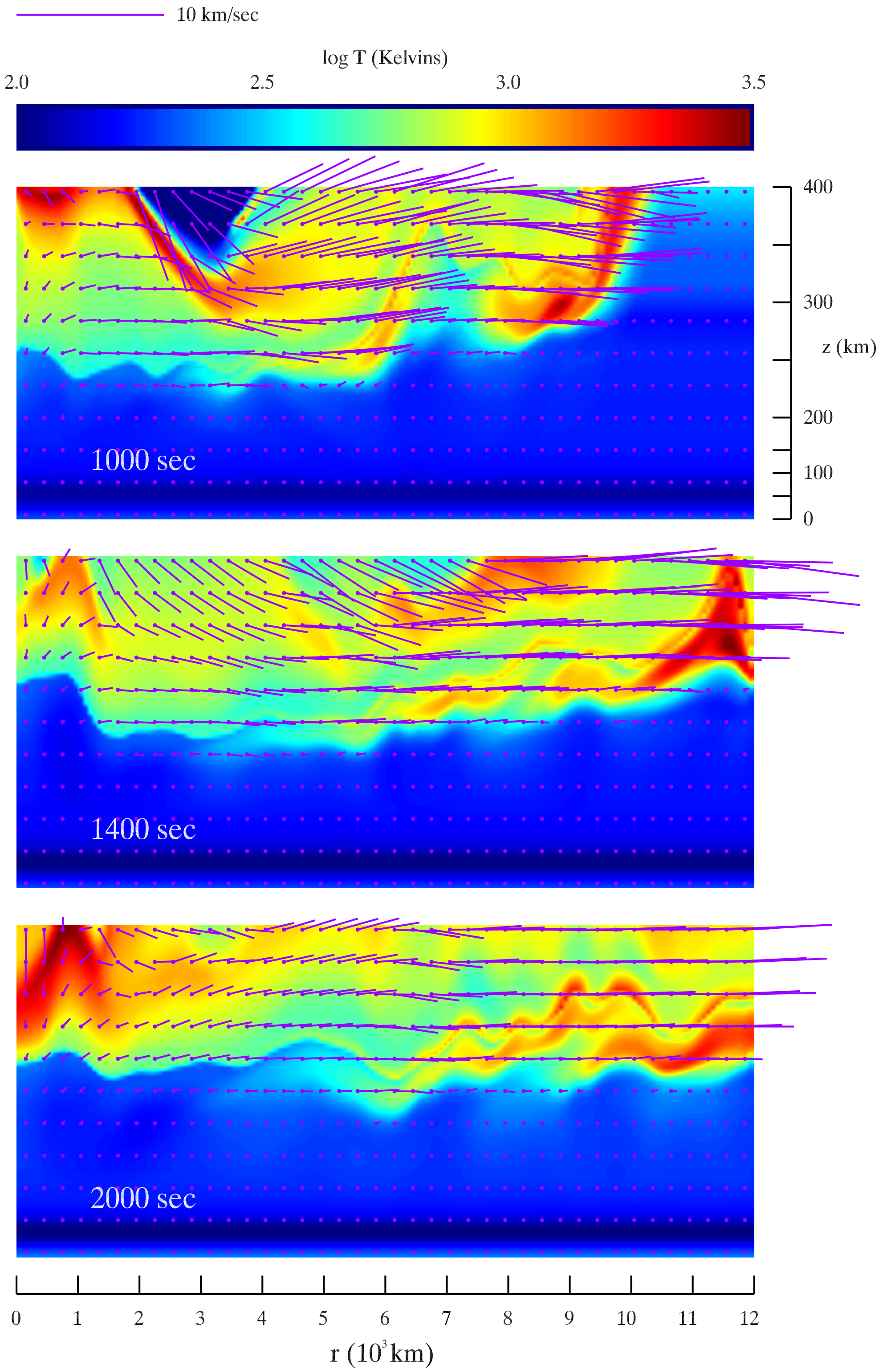

FIG. 4.— Temperature and velocity in the splashback of a large impact (e.g., L) at three times after the peak of the main event.

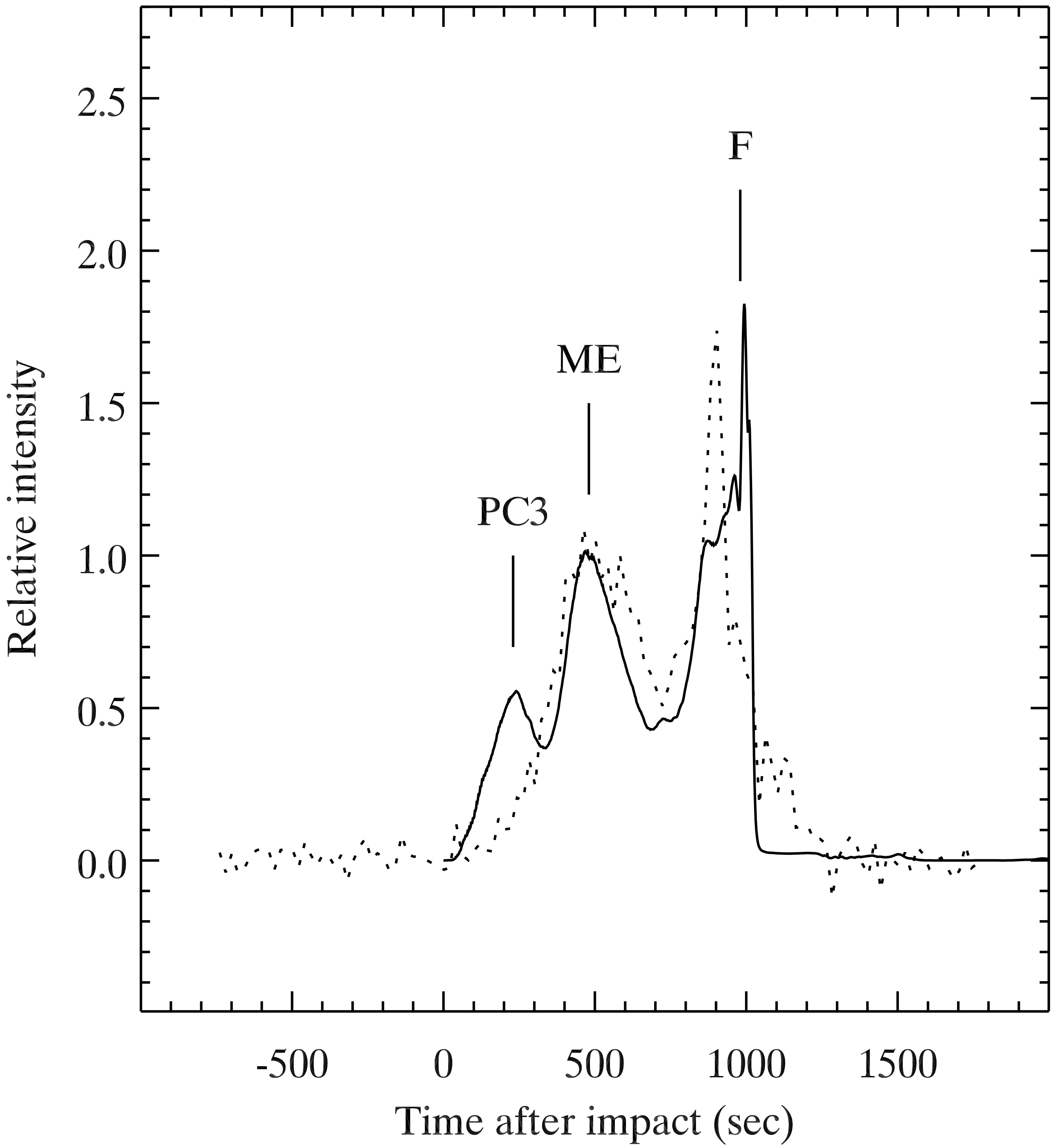

FIG. 5.— Observed light curve (dotted line) of the L impact at 0.9 μm, from Schleicher et al. (1994), in comparison to our modeled light curve at this wavelength (solid line). The modeled curve has been normalized in intensity to equal the observed curve at 450 sec. The notations PC3, ME and F stand for third precursor, main event, and flare, respectively.

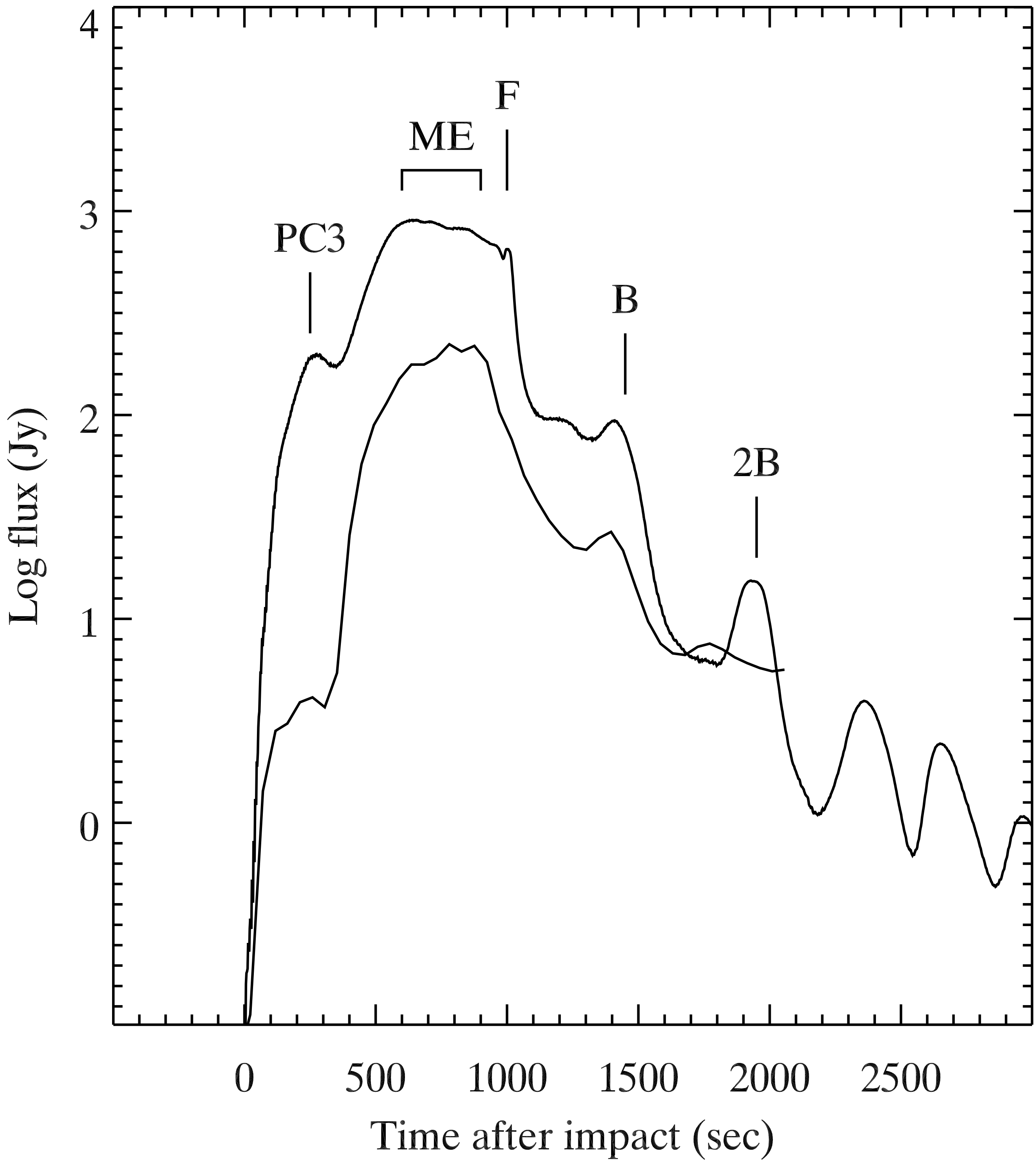

Fig. 6.— Observed light curve (lower plot) of the G impact at 2.3 μm, from McGregor et al. (1996), in comparison to our modeled light curve at this wavelength. The modeled curve has been offset upward for clarity. The notations PC3, ME, F, and B, and 2B stand for third precursor, main event, flare, bounce, and second bounce, respectively.

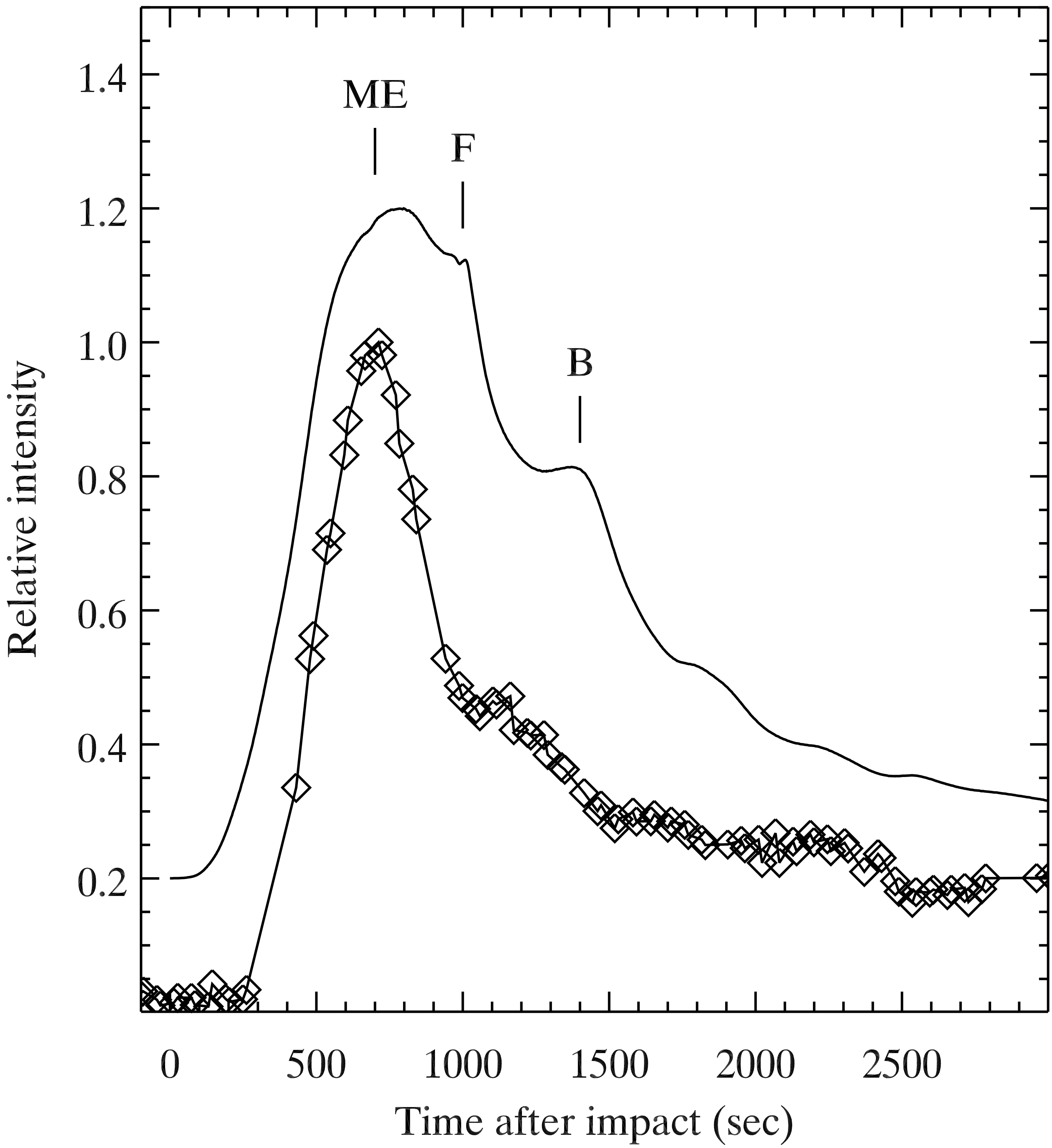

FIG. 7.— Observed light curve (lower plot, with points) of the H impact at 12 μm, from Lagage et al. (1995), in comparison to our modeled light curve, offset in the ordinate for clarity. The ‘F’ marks a residual flare feature in the modeled curve, and ‘B’ marks the first bounce.

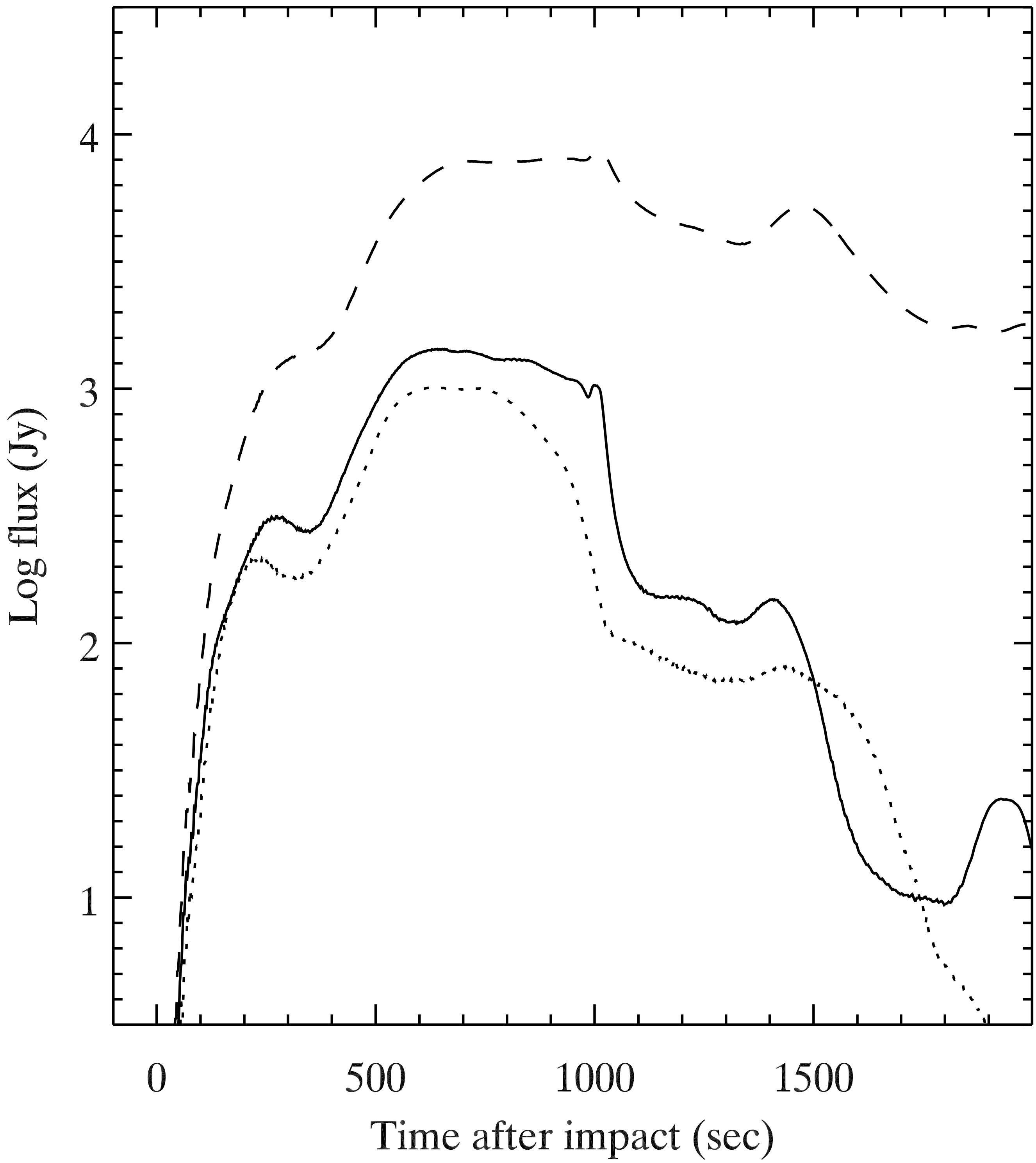

FIG. 8.— Effect of radiative damping, and omission of the vanguard, on light curves for a large impact (e.g., L) at 2 μm. The solid curve is the nominal plume model, including radiative damping and a vanguard. The dashed line shows the effect of turning off radiative damping, and the dotted line shows the effect of eliminating the vanguard.

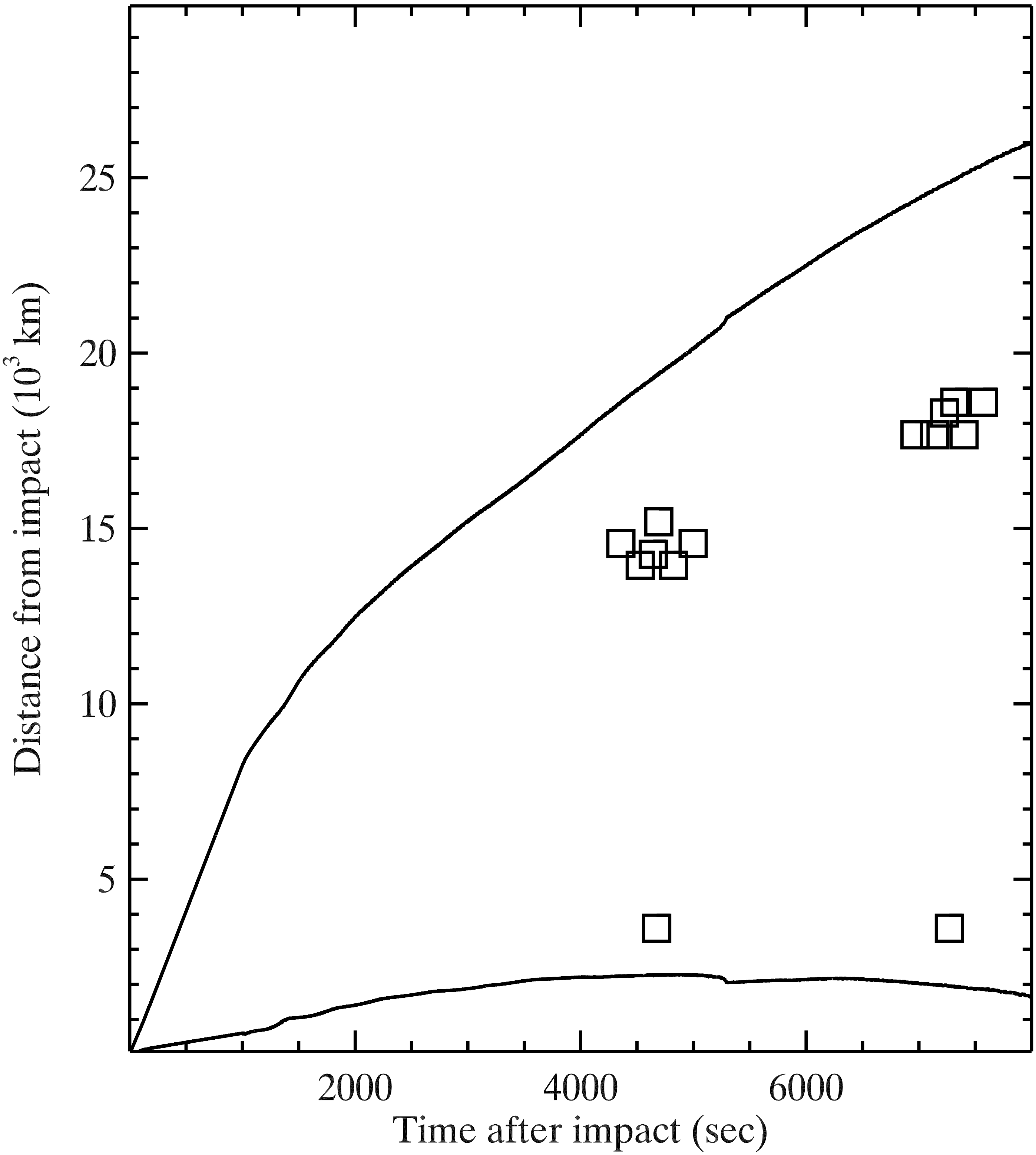

FIG. 9.— Observed radii (upper points) and offset (lower points) of the 3–4-μm ring from G and K impact data by McGregor et al. (1996), in comparison to the modeled radii (upper curve) and offset (lower curve) versus time.